Laitinen, Alpo; Korhonen, Marko; Keskinen, Karri; Kaario, Ossi; Vuorinen, Ville

Large-eddy simulation of buoyant airflow in an airborne pathogen transmission scenario

Published in:
Building and Environment

DOI:
10.1016/j.buildenv.2023.110462

Published: 01/08/2023

Document Version
Publisher's PDF, also known as Version of record

Building and Environment 241 (2023) 110462

Contents lists available at ScienceDirect

Building and Environment

journal homepage: www.elsevier.com/locate/buildenv

Large-eddy simulation of buoyant airflow in an airborne pathogen transmission scenario

Alpo Laitinen *, Marko Korhonen, Karri Keskinen, Ossi Kaario, Ville Vuorinen

Department of Mechanical Engineering, Aalto University, Otakaari 4, P.O. Box 14100 FI-00076 AALTO, Espoo, Finland

ARTICLE INFO

Keywords:
Large-eddy simulation (LES)
Airborne virus
SARS-CoV-2
Indoor airflow
Natural convection
Buoyancy

ABSTRACT

Indoor airflow patterns and the spreading of respiratory air were studied using the large-eddy simulation (LES) computational fluid dynamics (CFD) approach. A large model room with mixing ventilation was investigated. The model setup was motivated by super-spreading of the SARS-CoV-2 virus with a particular focus on a known choir practice setup where one singer infected all the other choir members. The room was heated with radiators at two opposite walls in the cold winter time. The singers produced further heat generating buoyancy in the room. The Reynolds number of the inflow air jets was set to $Re = 2750$, corresponding to an air-changes-per-hour (ACH) value of approximately 3.5. The CFD solver was first validated after which a thorough grid convergence study was performed for the full numerical model room with heat sources. The simulations were then executed over a time of $t = 20$ min to account for slightly more than one air change timescale for three model cases: (1) full setup with heat sources (radiators+singers) in the winter scenario, (2) setup without radiators in a summer scenario, and (3) theoretical setup without buoyancy (uniform temperature). The main findings of the paper are as follows. First, the buoyant flow structures were noted to be significant. This was observed by comparing cases 1/2 with case 3. Second, the dispersion of the respiratory aerosol concentration, modeled as a passive scalar, was noted to be significantly affected by the buoyant flow structures in cases 1–2. In particular, the aerosol cloud was noted to either span the whole room (cases 1–2) or accumulate in the vicinity of the infected singer (case 3). Turbulence was clearly promoted by the interaction of the upward/downward moving warmer/cooler air currents which significantly affected the dispersion of the respiratory aerosols in the room. The study highlights the benefits of high-resolution, unsteady airflow modeling (e.g. LES) for interior design which may consequently also impact predictions on exposure to potentially infectious respiratory aerosols.

1. Introduction

The COVID-19 pandemic has raised the general level of awareness on the indoor air quality due to the transmission of the SARS-CoV-2 virus as small airborne particles i.e. aerosols [1–3]. In fact, several key international organizations, such as the World Health Organization (WHO) and the American Society of Heating, Refrigerating and Air-Conditioning Engineers (ASHRAE), mention the improvement of indoor air quality via ventilation and air filtration as major mitigation measures for virus transmission [4–6]. In the present work, scale-resolving computational fluid dynamics (CFD) simulations are carried out in order to better understand the physics of indoor airflows relevant to long-distance virus transmission encountered in super-spreading events [7].

In a previous numerical study, Borro et al. [8] utilized computational fluid dynamics (CFD) simulations in order to understand the role of heating, ventilation and air conditioning (HVAC) on the dispersion of the virus in a hospital environment using Reynolds-Averaged Navier–Stokes (RANS) turbulence modeling. They modeled the virus transport as Lagrangian particles in addition to a passive scalar from the infected source. They reported that doubling the ventilation rate reduced the aerosol concentrations but increased and sped-up the long distance contamination due to increased turbulence. Such time-averaged CFD simulations could be used to predict the risk of contagion in indoor environments. Blocken et al. [9] conducted an experimental study on the effect of ventilation and air cleaning to the aerosol concentration at a gym with 35 people. They found that the combination of the existing ventilation in the building with an additional air cleaning reduced the aerosol concentration in the air by up to 90%. Ren et al. [10] investigated three different ventilation strategies in a COVID-19 inpatient

* Corresponding author.
E-mail addresses: alpo.laitinen@aalto.fi (A. Laitinen), marko.korhonen@aalto.fi (M. Korhonen), karri.keskinen@aalto.fi (K. Keskinen), ossi.kaario@aalto.fi (O. Kaario), ville.vuorinen@aalto.fi (V. Vuorinen).

https://doi.org/10.1016/j.buildenv.2023.110462
Received 17 March 2023; Received in revised form 17 May 2023; Accepted 26 May 2023
Available online 2 June 2023

ward numerically using CFD employing RANS modeling. They noted that the location of the exhaust vents may pose a crucial role in the removal of aerosols.

Ascione et al. [11] explored the usage of CFD with RANS in the designing of HVAC systems for safe classrooms in educational buildings. They pointed out the importance of the HVAC design on the overall safety of the classrooms. Deng et al. [12] studied both numerically with CFD and RANS as well as experimentally the spreading of aerosols in a breathing micro-environment under stable, neutral and unstable air stability conditions. They noted that the most suitable ventilation method depends on the air stability. Bhattacharyya et al. [13] examined numerically with CFD and RANS the spreading of aerosol sanitizer in a hospital room. They observed that the level of turbulence increases the dispersion of the sanitizer in the room.

As also discussed above, indoor airflow CFD simulations have been carried out extensively in the past [14]. However, most of the previous simulations have utilized RANS methods in contrast to large-eddy simulations (LES) [15]. LES is a method where the large scale turbulence is directly resolved and only the sub-grid scale (SGS) is modeled. While LES is considered to be physically more accurate than RANS, the accuracy comes at a significant increase in the computational cost. Moreover, the accuracy of LES is highly dependent on the used grid resolution. Jiang et al. [16] investigated a full-scale room with ventilation using LES for airflow ranging from 0.1 to 27.9 ACH. They reported counter gradient transport using LES when ACH was higher than 1. Such phenomenon may not be predicted by RANS models that are based on gradient transport assumptions, which partly explains why accurate predictions are difficult to obtain using RANS. Liu et al. [17] modeled Lagrangian particles in an indoor environment using LES and RANS. LES was noted to predict more accurately the concentration fluctuations during particle emission. However, in the long-term exposure both methods provided mostly similar results. Karadimou et al. [18] modeled Lagrangian particles with two-way coupling in a ventilated room using LES and RANS. They observed higher accuracy of LES in recirculation regions. Vuorinen at al. [1] modeled the dispersion of aerosols with LES in indoor spaces. Also Monte Carlo simulations were utilized to assess the role of different parameters, including the number of persons, air changes per hour, loudness of speaking etc., on the virus exposure via aerosol particles. Published in mid 2020, their study was among the first multidisciplinary, computational assessments on the airborne transmission of COVID-19. Liu et al. [19] simulated a real-life restaurant setting with LES where people exposed to COVID-19 were infected. They reported a strong link between the high aerosol concentrations and the infection pattern reported from the setting.

The inflow airflow in mechanical ventilation simulations is commonly modeled as an air jet. Air jets are inherently unsteady, advocating the usage of LES in such simulations. In jet modeling context, Tu et al. [20] examined opposing planar jets experimentally and numerically using LES. They noted that for such flows, scale-resolving models are necessary to capture the unsteady phenomena. Thysen et al. [21] compared LES and different RANS models for jet flows in a room with mixing ventilation. They reported that RANS models fail to accurately predict the mean flow characteristics of the jet-jet impingement zone.

In natural ventilation, the airflow is driven by buoyancy. Such buoyancy-driven flows are generally considered to be inherently unsteady [22], advocating the usage of transient, scale-resolving simulations, such as LES. Huang et al. [23] investigated the turbulent characteristics of mixed convection in a rectangular cavity using LES. The accuracy of LES was confirmed by comparing the numerical results with experiments. Chew et al. [24] simulated natural ventilation in a building with LES to provide new correlations for the convective heat transfer and natural ventilation flow rates. The new correlations differed significantly from the standard ones, and were able to predict accurate indoor air temperature and surface temperatures when compared with experiments. Durrani et al. [25] evaluated the performance of LES and unsteady RANS (URANS) in predicting multiple steady states in natural ventilation. LES was noted to predict more accurately the temperature levels in the building, while URANS failed to predict unsteadiness in the flow. Caciolo et al. [26] compared RANS and LES in single-sided natural ventilation, and the numerical results were compared to available experimental data. They reported better capturing of the turbulent characteristics and overall more accurate results with LES, however, with significantly higher computational cost. Auvinen et al. [27] studied the effect of air purifiers and space dividers on aerosol transmission in a restaurant using LES. They reported that turbulent mixing has a crucial role in fast dispersion of the concentration peaks. Such mixing would be promoted using air purifiers decreasing the risk of infection and level of virus exposure. Space dividers alone were noted to not reduce the risk of infection.

Based on the presented literature survey, there is a clear research gap on publications of simulations involving mixing ventilation combined with strong buoyancy-driven flows using LES. Furthermore, various previous studies have provided evidence on the demand to resolve the flow scales using LES type methods (see e.g. [23,25,26]). Here, we simulate a large model room with mixing ventilation. The room is heated by thermal radiators and humans acting as heat sources generating thermal plumes. Along with numerous super-spreading events reported during COVID-19, the studied set-up is motivated by a real-life choir practice event where a single individual infected everyone else in the room despite of social distancing and practiced hand hygiene. First, in addition to our earlier validation and verification studies in other flow setups [28,29], we first validate the used CFD code. The main objectives of this paper are then formulated as follows. First, assess the flow patterns generated by the ventilation and heat sources. Second, assess the transmission of the respiratory aerosol particles, modeled as a passive scalar, in a few flow scenarios.

2. Methods

2.1. Case set-up

The case studied here is a large room (12 m × 12 m × 3 m) with mixing ventilation. The setup is mainly motivated by a choir practice event where one of the individuals infected the other choir members. A schematic picture of the simulation domain can be seen in Fig. 1. Fresh air enters the room at $T_{in} = 19°C$ at a velocity of $U_{in} = 0.105$ m/s (i) from the ceiling corresponding to 3.5 air changes per hour (AC H= 3.5 1/h). The exhaust vents (ii) are set to identical size compared to the inflow vents. The inflow and exhaust vents are both modeled as elongated gaps through which the air enters or exits the room. The room is being heated by the radiators (iii) and the humans (v), which are modeled as volumetric heat sources. A total of eleven people (v) are in the room next to long tables (iv). The more specific dimensions in the domain can be seen in Fig. 1(b). From the 11 people in the room, 9 are singers (vii) gathered in the three rows on the upper side of the picture, while the choir leader (viii) and the musician (ix) are located on the lower part of the room. The infected singer is located in the upper right corner of the figure (vi). The exact measures of the dimensions are shown in Table 1. The height and thickness of the tables are $h = 0.8$ m and $w_t = 0.1$ m, while the height of the radiators is $H = 0.6$ m and the radiators are elevated 0.2 m from the floor. The thermal sources are modeled as heated volumes and not as solid objects, i.e. flow is able to pass through them. In such a way, the large error due to under-resolving the thermal and viscous boundary layers can be avoided while the introduced heating power can be well-defined.

2.2. Governing equations

The fluid flow is governed by the conservation of mass, momentum and energy

$$\frac{\partial \rho}{\partial t} + \nabla \cdot (\rho \mathbf{u}) = 0 \tag{1}$$

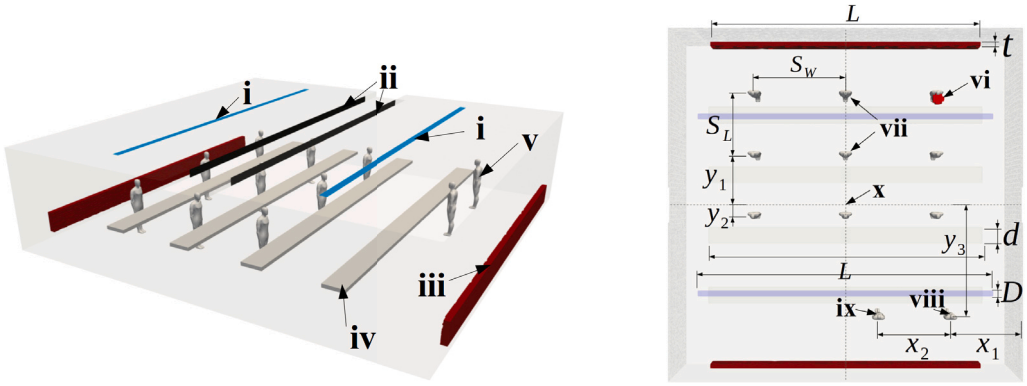

Fig. 1. (a) A schematic of the computational domain. i: inflow air vents, ii: exhaust air vents, iii: radiators, iv: tables, v: singers. (b) Dimensions of the domain. vi: aerosol source i.e. the infected singer, vii: healthy singers, viii: choir leader, ix: musician, x: center-lines (dashed lines). S_W: lateral distance between the singers, S_L: longitudinal distance between the singers, L: the length of the tables, radiators and inlet channel, t: thickness of the radiator, d: width of the tables, D: width of the inlet, y_1: distance of the second row of singers from center-line, y_2: distance of the first row of singers from the center-line, y_3: longitudinal distance of the choir leader and the musician from the center-line, x_1: lateral distance of the choir leader from the wall, x_2: lateral distance between the choir leader and the musician.

Table 1
The detailed dimensions used in the domain.

Symbol	Measure	Distance (m)
S_W	Lateral distance between singers	3.3
S_L	Longitudinal distance between the singers	2.2
L	Length of the radiators, tables and inlet	10
t	Thickness of the radiator	0.15
d	Width of the tables	0.6
D	Width of the inlet	0.2
y_1	Distance from the center-line to the second row of singers	1.7
y_2	Distance from the center-line to the first row of singers	0.5
y_3	Distance from the center-line to the choir leader and the musician	3.9
x_1	Distance from the wall to the choir leader	2.2
x_2	Distance between the choir leader and the musician	2.6

$$\frac{\partial}{\partial t}(\rho\mathbf{u}) + \nabla\cdot(\rho\mathbf{u}\mathbf{u}) = -\nabla p + \rho g + \nabla\cdot(2\mu_{eff}D(\mathbf{u})) - \nabla\left(\frac{2}{3}\mu_{eff}(\nabla\cdot\mathbf{u})\right) \quad (2)$$

$$\frac{\partial}{\partial t}(\rho h)+\nabla\cdot(\rho\mathbf{u}h)+\frac{\partial}{\partial t}(\rho K)+\nabla\cdot(\rho\mathbf{u}K)-\frac{\partial p}{\partial t} = -\nabla\cdot\mathbf{q}+\nabla\cdot(\boldsymbol{\tau}\cdot\mathbf{u})+\rho r+\rho\mathbf{g}\cdot\mathbf{u} \quad (3)$$

where ρ is the density, t is the time, $\mathbf{u}$ is the velocity vector, p is the pressure, g is the gravitational constant, μ_{eff} is the sum of molecular and subgrid-scale (SGS) eddy viscosity, $D(\mathbf{u}) = \frac{1}{2}(\nabla\mathbf{u} + (\nabla\mathbf{u})^T)$ is the strain rate tensor, h is the sensible enthalpy, K is the mass specific kinetic energy, $\mathbf{q}$ is the heat flux, r is a mass specific heat source, $\rho\mathbf{g}\cdot\mathbf{u}$ is the rate of change of potential energy, and $\nabla\cdot(\boldsymbol{\tau}\cdot\mathbf{u})$ is a mechanical energy source, which here corresponds to the conversion of mechanical energy to heat by the viscous forces. The fluid here is air which is considered to be compressible due to density changes via temperature variations. The density of the fluid is calculated from the ideal gas law

$$\rho = \frac{p}{RT} \quad (4)$$

where T is the temperature and R is the specific gas constant. The passive scalar concentration is governed by the convection–diffusion equation

$$\frac{\partial c}{\partial t} + \mathbf{u}\cdot\nabla c = D\nabla^2 c \quad (5)$$

where c is the scalar concentration and D is the diffusion constant. In the present work, the unity Schmidt number ($Sc = \nu/D$) assumption is made, i.e. $Sc = 1$.

2.3. Numerical approach

Here, we utilize the OpenFOAM open-source CFD software based on the finite volume method (FVM) [30]. The `buoyantPimpleFoam` solver is used to account for the buoyant effects induced by temperature variations. The solver has been previously validated by the authors in a turbulent channel flow setup [28]. Further validation and verification are provided in Appendix A and Appendix B. The solver was also recently used by the authors [29] to simulate droplet dispersion in air induced by strong air jets in a kraft recovery boiler context. The `buoyantPimpleFoam` solver is based on the PIMPLE algorithm, which is a combination of the unsteady PISO [31], and steady state SIMPLE [32] algorithms. The convection term of the momentum equation as well as all the diffusion terms are discretized using the linear central differencing scheme. For the convection of the scalar equations, a second order accurate flux limiter is used with the Total Variation Diminishing (TVD) property [33]. For temporal discretization, a second order accurate implicit scheme is used.

The sub-grid scale turbulence is modeled by the k-equation LES model [34]. In LES, the large scale flow is resolved on the computational grid, while the sub-grid scale effects are modeled. The k-equation model is a one-equation model where the sub-grid scale turbulent kinetic energy is governed by the equation

$$\rho\frac{\partial k}{\partial t} + \rho U_j\frac{\partial k}{\partial x_j} = \tau_{ij}\frac{\partial U_i}{\partial x_j} - \frac{\rho C_e k^{3/2}}{\Delta} + \frac{\partial}{\partial x_j}\left[(\mu+\mu_T)\frac{\partial k}{\partial x_j}\right] \quad (6)$$

where eddy viscosity is defined as $\mu_T = \rho C_k \Delta\sqrt{k}$. The filter parameter $\Delta = V_c^{1/3}$ depends on the cell volume V_c, and the constant parameters are $C_k = 0.094$ and $C_e = 1.048$, which are the default values in OpenFOAM. These parameters are consistent with our previous study [29].

2.4. Boundary conditions and simplifications

The inflow of air is modeled as two large low-velocity air jets that create air curtains. The inflow air velocity is set to $U = 0.105$ m/s, which corresponds to an inlet Reynolds number of $Re = UD_h/\nu = 2750$, referred to the hydraulic diameter of the inlet channel ($D_h = 4LD/(2(L+D)) \approx 0.39$ m), and air-changes-per-hour value of $ACH = 3.5\ 1/h$. For computational feasibility, the simulations are carried out for a physical time of t =20 min, which corresponds to slightly more than one air change time scale. The inflow air temperature is set to $T = 19°C$. The outlets are modeled with a boundary condition that prevents reverse flow. Here, the walls are considered adiabatic for simplicity i.e. heat transfer from the walls is not taken into account. However, the wall function by Launder and Spalding [35] is applied to the turbulent viscosity.

The heat sources are modeled as volumetric heat sources. The radiators heat the room at power $P = 720$ W each while each of the humans release heat at the power $P = 60$ W. The power of the radiators is based on the heating requirement of a passive house (10 W/m^2) [36], since the domain walls are set adiabatic. An average person produces heat in the order of $P = 120$ W while standing [37]. In the present study, half of this power is assumed to be radiation heat transfer, and hence, the value of $P = 60$ W is used. As a remark, the radiated heat is less localized and hence it may be considered to have less effect on the thermal plume formation. Thereby, the heat radiation effects are ignored herein. With these choices the average steady state room temperature stays around a typical indoor air temperature (e.g. 21-23 °C). The heat from the singers corresponds to an estimate of the net power from the convective heat transfer as well as the heat from the exhaled air. The exact values of the heat sources are modeling assumptions. The radiators and humans are not modeled as solid surfaces, i.e. air may flow through them. In reality, human body is not a stationary obstacle and the clothing and motion further complicate modeling the near-surface viscous/thermal boundary layers. Here, the volumetric heat source modeling approach was chosen to avoid the under-resolving and modeling of the convective heat transfer (viscous and thermal boundary layers) on the surfaces. This allows the implementation of the exact amount of heat to the system without resolving the wall boundary layers of the heated bodies. Our assumption is that these buoyancy-driven flows are more dependent on the heating power rather than the exact geometry of the heated object which is unknown.

In the present work, the main focus is on relatively small aerosols that are able to transport over extended time and distance. The spreading of such respiratory aerosol particles is modeled as a passive scalar concentration (c) from a spherical source ($r = 0.2m$) at the location of the infected singer's breathing zone (see Fig. 1(b)). The passive scalar only accounts for the fine aerosols as the larger droplets are expected to be less involved in the airborne transmission of the virus [1]. Such fine aerosols may pose a dry particle size range in the order of e.g. $d \sim 0.1 - 30$ μm (depending on e.g. the airflow and relative humidity [1]) and they may remain airborne over extended time and distance. Such fine aerosols may be considered rather immune to gravitational effects. Here, the aerosol cloud is modeled as a continuous scalar concentration field. We set $c = 1$ inside the source while $c = 0$ initially outside the source. The airflow created by breathing or singing is considered to be relatively insignificant compared to the flow induced by the thermal plume of the singers. In addition, the airflow created by singing could be characterized as a pulsating, unsteady phenomenon, where the shape of the mouth and the song affects the breathing rate and direction. We do not resolve the mouth region due to the large scale separation between the mouth and the full interior scales (e.g. 1 mm vs 10 m). Based on our numerical testing, we consider that modeling the exhalation as an under-resolved flow, e.g. as a constant speed or oscillating jet, could generate a non-physical flow field around the singer. Hence, the airflow from respiratory activities is neglected here. The spherical aerosol source is large enough to intersect with the thermal plume as well as the cooler regions in the breathing zone. Consequently, all the aerosols in the breathing zone do not immediately rise vertically but part of them may also disperse horizontally outside the immediate breathing zone.

3. Results and discussion

3.1. General considerations

First, the used numerical model was validated against a canonical reference case i.e. thermally driven flow in an elongated cavity with heated walls [38]. The validation results are presented in Appendix A and the results of the turbulent 3D validation case encourage the usage of the model in the present simulations. Second, the numerical model was also verified by performing a grid independence study. A total of four different computational meshes were analyzed and the present mesh was chosen based on the results. In particular, the Pope criterion [39] was used to judge the adequate mesh quality for the present study. The details of the mesh in addition to the mesh independence study are presented in Appendix B. Based on the results of the grid sensitivity study, the mesh with 13.2M grid points is used for the present study. The sizes of cells varied between $\Delta x = 0.025$ m and $\Delta x = 0.00625$ m. With this mesh, the y^+ values at the walls remained below 5 on the average, except for the walls with the radiators where the average values were approximately 15. Third, a comparison between the present OpenFOAM solver and the DNSLABIB solver [40] under isothermal conditions is presented in Appendix C to further verify the numerical solution.

3.2. Global flow and thermal structures

The global flow features in the indoor flow configurations are presented on a set of cut-planes. The cut-plane locations can be seen in Fig. 2. The planes are referred to as planes A, B, C, and D. Note that the plane shown previously in the grid sensitivity analysis in Appendix B was plane B. Planes A, B and C intersect with the singer locations, while plane D coincides with the choir leader. The singers are not present in the simulations as solid objects, but they generate buoyancy as modeled volumetric heat sources. However, the singers are shown in the figures as manikins for better visual understanding.

3.2.1. Case 1: baseline set-up in a winter scenario

First, we investigate the full baseline set-up in the winter scenario with all heat sources activated. Fig. 3 illustrates streamlines in addition to the time-averaged flow field on the selected cut-planes. The human manikins are added to the figures for visual purposes. The air is noted to flow upward from the radiators (i) and the humans (ii). The flow speed is observed to be the highest at the radiators with peak velocities of ≈0.4 m/s. The air from the radiators and humans near the left walls (humans 1, 2 and 3) mix with the inflow air generating vortices in the upper corners of the room (iii). The tables are noted to generate further vortices in the wake regions (iv). Furthermore, the mixing of the downward flowing cool air with the upward flowing warm air generate vorticity in the mixing zone (v). On plane D, it is noted that on the left hand side of the room, the inflow and the buoyant flow from the radiator form a very large scale vortex (vi). This vortex is formed due to the absence of other heat sources between the inflow and the radiator that would generate opposing air streams, as compared to the smaller scale vortex (v) formed between the singer and the inflow in planes A, B and C. The choir leader and the inflow in plane D also create a large scale vortex (vii) due to the mixing of the cool and warm airs. It is noted that upward rising air plumes in the buoyant flows interact with the downward flow from the inlets which result in bending of the inflow jets (viii) towards the outlets.

The instantaneous temperature field is shown in Fig. 4. The flow near the walls is noted to become unstable and turbulent (i) due to

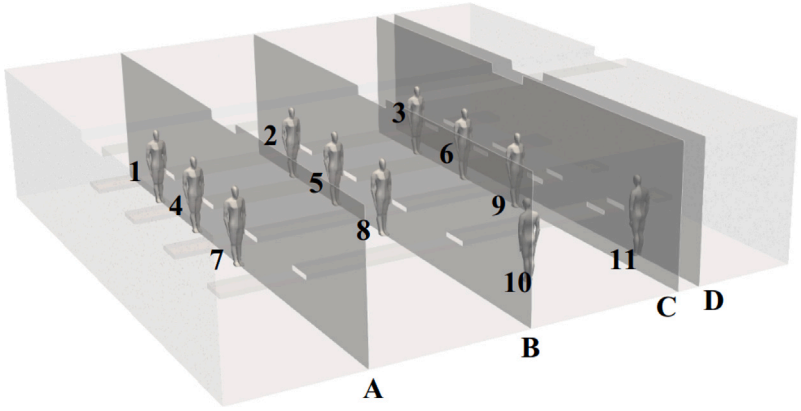

Fig. 2. Illustration of the different cut-planes over which the results of the main flow characteristics are shown in addition to the numbering of the singers in the room.

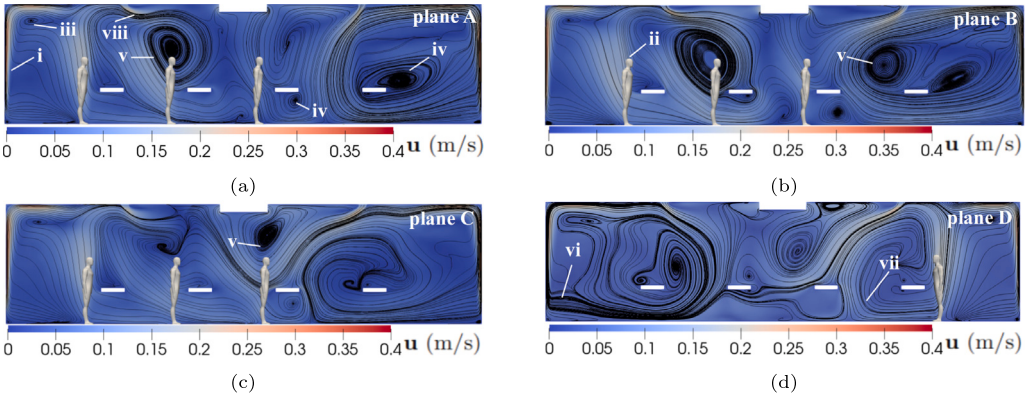

Fig. 3. Case 1: Illustration of the streamlines in the different cut-planes with the time-averaged velocity. (a) plane A, (b) plane B, (c) plane C, and (d) plane D. i: buoyant upward flow induced by the radiators, ii: thermal plume induced by the singers, iii: vortex induced by the interaction of the buoyant flows with the inflow, iv: coherent vortex structures in the wake regions of the tables, v: vortices induced by the mixing of the downward cool air and the upward warm air, vi: large scale vortex induced by the inflow and the radiator, vii: large scale vortex induced by the inflow and the choir leader, viii: bending of the inflow jets.

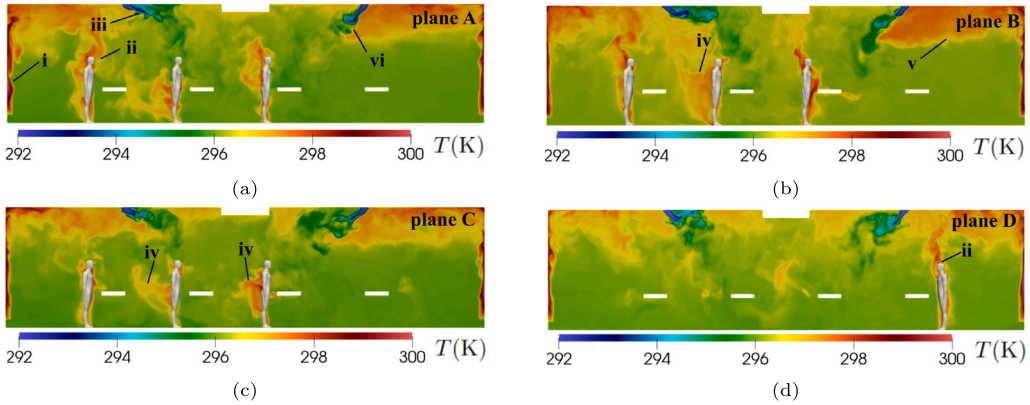

Fig. 4. Case 1: Illustration of the instantaneous temperature field in the different cut-planes. (a) plane A, (b) plane B, (c) plane C, and (d) plane D. i: heating from the radiator, ii: strong upward buoyant flow, iii: shear layer of the inflow, iv: inflow passing by the singers, v: thermal stratification, vi: mixing zone of the inflow air and the heat from the radiators.

the rising warm air from the radiators. The strength of the thermal plumes from the singers is noted to depend on the airflow and mixing characteristics near the persons. For example, the thermal plumes of the humans near the left and right walls (ii) on planes A-D (humans 1, 2, 3 and 11) are qualitatively noted to be the strongest. The shear layer of the inflow air is noted to be unstable (iii). However, due to the low Reynolds number and buoyancy-driven flow character, a classical Kelvin–Helmholtz instability is not observed. The inflow is observed to pass by the singers 4, 5 and 6, who are closer to the inflow region, with observed average peak velocities in the order of 0.2 m/s (iv). In reality, such cool flow would already be felt by the singers resulting potentially in thermal discomfort. Here, in Case 1, thermal stratification (v) is noted near the ceiling as a zone of warmer air of approximately 25 °C while otherwise the average room temperature is about 22-23 °C away from the singers. In an ideal mixing ventilation scenario, the temperature should be mostly uniform. However, in contrast, thermal

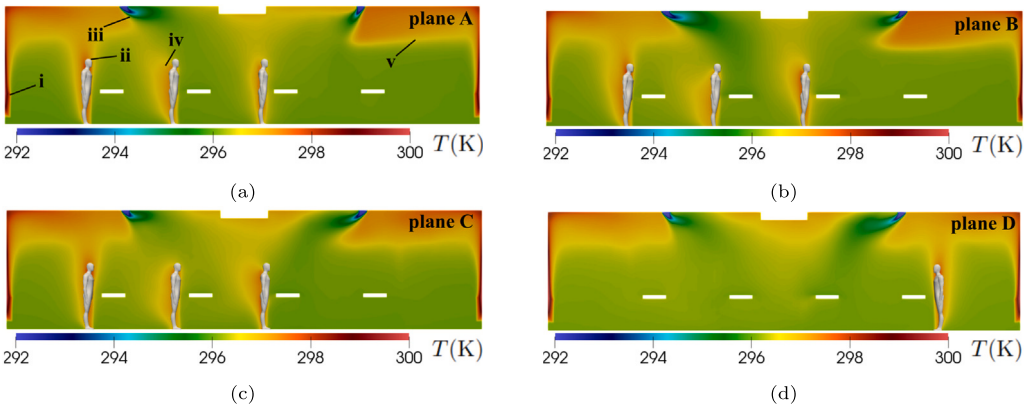

Fig. 5. Case 1: Illustration of the time-averaged temperature field on the cut-planes. (a) plane A, (b) plane B, (c) plane C, and (d) plane D. i: Heating from the radiator, ii: upward buoyant flow, iii: inflow, iv: inflow passing by the singers, vi: bending of the inflow jets, and v: thermal stratification.

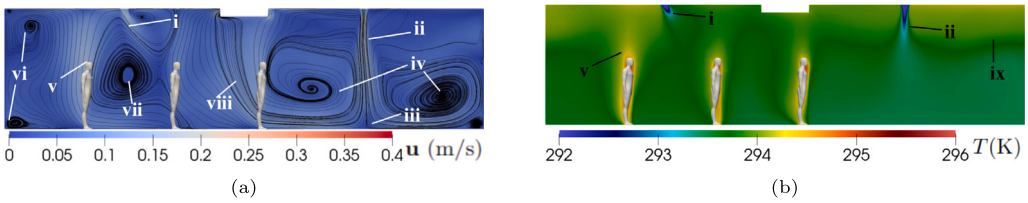

Fig. 6. Case 2: Visualization of (a) streamlines with the time-averaged velocity cut-plane, and (b) time-averaged temperature field of the case without tables and radiators from plane B. i: Slight bending of the left hand inflow, ii: little to no bending of the right hand inflow, iii: impingement of the inflow jet, iv: vortices induced by the impingement of the inflow jet, v: thermal plume from the singer, vi: corner vortices, vii: vortex induced by the mixing of the thermal plumes and the inflow air, viii: slight bending of the thermal plume towards the outlet, ix: thermal stratification.

stratification is clearly noted in the present Case 1. Furthermore, mixing of the cold inflow jets with the stratified warm air is noted close to the ceiling (vi). Such effect may potentially recirculate the stale air instead of exchanging it with the fresh air. Fig. 5 shows the time-averaged temperature field confirming the observations in Fig. 4.

In conclusion, the baseline case 1 poses highly rich physics and complex flow structures which are formed due to the interaction between the thermal plumes and mechanical ventilation. The flow features indicate that the heat sources may have a high impact on the overall flow field structure. The inflow air jet is significantly bent by the buoyant flow induced by the radiators and the humans. Hence, accurate prediction of the temperature fields is of great importance in obtaining realistic results. Here, the utilization of scale-resolved LES is considered necessary in order to capture the rich flow physics.

3.2.2. Case 2: empty room in a summer scenario

Next, we simulate another flow scenario of the same room in a more generic summer setup. In this case 2 scenario, now the simulation is carried out without heating from the radiators while the singers still act as heat sources. In addition, the tables in the room are removed to account for a more general empty room scenario. The configuration of the singers is maintained the same as in case 1. The main purpose of case 2 is to offer insight to flow sensitivity related to seasonal heating.

The streamlines and the time-averaged velocity field and temperature fields on plane B (see Fig. 2) are illustrated in Fig. 6. It is observed that due to the absence of the radiators, the left inflow is bent but clearly less than in case 1 (i). However, the bending of the right inflow remains negligible (ii), hence creating a vertical air curtain in the room. The right inflow impinges on the floor (iii), inducing coherent vortices in the shear regions (iv). Qualitatively, the thermal plumes from the singers (v) are noted to be more persistent and upward-biased with less bending. Due to the absence of the radiators, the turbulence level in the room is also noted to be lower in case 2. Furthermore, coherent corner vortices are observed as well (vi). In zone (vii), the thermal plumes and the inflow interact inducing a large scale vortex. In contrast to case 1 where a respective vortex was observed (see Fig. 3), the present vortex is now observed between the two singers. The thermal plume of the singer closest to the outlets is noted to be slightly bent (viii) towards the outlet. Thermal stratification (ix) is observed even without the radiators. As a conclusion from cases 1-2, the configuration of the thermal sources, ventilation inlets and exhausts as well as the number of people in the room may have a significant effect on the overall flow patterns.

3.2.3. Case 3: case 1 under isothermal flow assumption

In case 3, we simulate exactly the same geometrical room configuration as in case 1 i.e. room with tables. However, now all the volumetric heat sources are deactivated resulting in a uniform temperature field of 19 °C. Hence, buoyancy effects are neglected and the flow is solely driven by the mechanical ventilation. Similar to cases 1-2, the singers are not physically present in the simulations. However, their locations are visualized as manikins in the following figures. The main purpose of case 3 is to indicate the effect of temperature variations to the overall flow field with particular relevance to case 1.

The instantaneous and time-averaged velocity fields and the streamlines on plane B are illustrated in Fig. 7. The inflow enters as a laminar jet (i) and impinges at the floor (ii). The jets are slightly bent towards the outlets and the two jets mix in the center of the room creating turbulence (iii). The inflow jets generate large scale vortices (iv) in the room. The tables are noted to slightly perturb the large vortex structures (v).

The overall flow structures in cases 1-3 are noted to be strongly affected by the combined effect of the heat sources. Based on our numerical tests, the tables are considered to be less important in the formation of the overall flow patterns and they are noted to act more as a local flow perturbation. The presence of buoyancy is noted to have the most significant effect on the flow characteristics in the room. Modeling indoor airflow without buoyancy (case 3) may thus be considered to

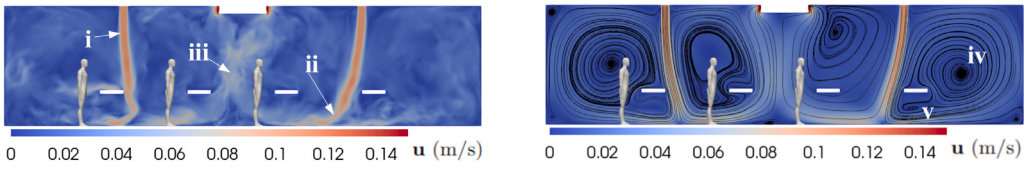

Fig. 7. Case 3: Visualization of (a) instantaneous velocity field and (b) streamlines with the time-averaged velocity field from plane B. i: the laminar inflow does not exhibit vortical structures in the shear layer, ii: the inflow jets bend slightly towards the outlets before impinging at the floor, iii: the mixed upward flow towards the outlets is seemingly turbulent, iv: the inflow induces large vortical structures in the room, v: the tables perturb the large vortical structures.

be unrealistic in the present setup while such isothermal flows may be more relevant to window ventilation scenarios with high ACH. The present numerical observations on the thermal stratification and airflow patterns indicate that the heating, furniture and number of people in the room may all have an effect on the complex flow patterns affecting also the indoor air quality.

3.3. Respiratory aerosol transmission from an infected source

As mentioned earlier, the present study was largely motivated by a choir practice super-spreading event where a single individual infected the other choir members. In the present work, we model the concentration of the fine respiratory aerosols as a passive scalar (c) which is transported by the air currents. The parameter c is dimensionless and it does not affect the fluid flow. Here, the focus is in particular on the fine aerosols (e.g. below a few tens of micrometers) that stay airborne for extended time and distance [1]. We set $c = 1$ inside the spherical source. Initially, $c = 0$ outside the source. The results for cases 1-3 are scaled so that the aerosol production rates are equal. The scaling is needed since the airflow at the source location varies between cases 1-3.

The dispersion of the aerosols is shown in Fig. 8 at t =1 min and t =20 min for the three cases. In cases 1 and 2, the thermal plume of the infected singer (i) is noted to transport the aerosol cloud strongly towards the ceiling resulting in primary concentration peaks. Subsequently, the inflow returns the high concentration part of the cloud downwards to the vicinity of the singer in the second row (singer 6) (ii). Furthermore, secondary concentration peaks are noted near the ceiling (iii). In case 1, the bending of the inflow jets pushes aerosols across the room all the way to the opposite side of the room towards the choir leader and the musician (iv) i.e. persons 10 and 11. In case 2, the air curtain induced by the rightmost inflow partially hinders the dispersion of the aerosols towards the choir leader and the musician (v). In case 3, the aerosol cloud remains highly concentrated near the infected singer and, in contrast to the buoyant cases 1-2, the cloud is now pushed upward by the large isothermal vortex (vi) which was also observed in Fig. 7(b). The aerosol dispersion in cases 1 and 2 is qualitatively rather similar, while the dispersion of the aerosols in case 3 remains relatively small and the aerosol cloud is not noted to reach the opposite end of the room. In contrast, in case 3 the concentration cloud stays relatively confined in the proximity of the infected singer.

In all cases, most of the aerosol cloud first travels upwards due to either buoyancy (cases 1-2) or a coherent flow structure (case 3). After that, part of the cloud returns back to the breathing level resulting in higher aerosol concentration below the inflow jets. The visualization of the aerosol concentration at the breathing level and the corresponding probability density function (PDF) for each case are shown in Fig. 9. The higher concentration of aerosols being pushed down by the inflow is clearly noted for cases 1 and 2 (i). The higher bending of the jets is noted to enhance dispersion of the aerosols transporting them longitudinally towards the choir leader at the opposite end of the room as noted in case 1 (ii). More lateral dispersion of the aerosols (iii) is noted in case 2 due to the air curtain hindering the longitudinal motion. In case 3, the air curtain from the inflow is noted to significantly hinder the dispersion in the longitudinal direction (iv). Thus, the exposure of the choir leader and the musician remains negligible in case 3. The PDF's for cases 1 and 2 indicate that the concentration is non-zero everywhere at the breathing level. This indicates higher level of mixing between the respiratory air of the infected person and the surrounding air. In case 3, the PDF shows that the concentration at the breathing level is mostly almost non-existent i.e. $\approx 50\%$ of the cells have $c \approx 0$ (see Fig. 9(e)). This indicates that the absence of turbulent flow structures in the vicinity of the infected person may limit the level of mixing. It is observed that the concentration cloud highly accumulates in the proximity of the infected singer in case 3.

The observations above are particularly well confirmed in Fig. 10 where the aerosol concentration fields for cases 1-3 are shown on planes C and B. Plane C cuts through the infected singer i.e. the leftmost person in the figure. The visualization indicates that the higher aerosol concentration that accumulates near the ceiling (ii) is pushed down by the inflow (i), creating a region of higher concentration around the singer below the inflow (singer 6). In case 2, an aerosol cloud is noted to be trapped in a corner vortex (iii) (observed in Fig. 6). In case 3 the concentration accumulates in the proximity of the infected singer (iv) and a higher aerosol concentration is trapped in the large isothermal vortex (v). It is noted from the figure by comparing the fields between planes B and C that the overall concentration level on plane C is much higher than on plane B. This further demonstrates our observation that the transport of the aerosols is much higher in the longitudinal direction (i.e. from the infected singer towards the choir leader) compared to the lateral. Next, we further consider the exposure level of the individuals in the room.

The average concentration of the respiratory aerosols as a function of time in the vicinity of the mouth of each singer is presented in Fig. 11. The local average concentrations are calculated over a sphere with a radius of r = 20cm centered at the head of each singer, representing the breathing zone. In addition, a total average concentration is shown along with an estimation of the equilibrium concentration level assuming perfect mixing (0D). The equilibrium concentration is calculated based on the numerical data of the volumetric average concentration. The temporal gradient of the source is evaluated in the beginning of the simulation, which corresponds to the rate of the exiting aerosol flux at steady state assuming perfect mixing. A concentration peak (i) is observed in cases 1 and 2 for the person 6 who is closest to the infected singer. Qualitatively, this was noted also in Fig. 8. In case 1, the highest concentrations are experienced by the singers in front of the infected singer, i.e. persons 6, 9 and 11, while the lowest concentrations were observed for the singers with the highest lateral distance from the infected singer (persons 1, 4 and 7). This is due to the observation that the strongest flow currents are in the vertical and longitudinal directions in the room, while little motion is noted in the lateral direction. In case 2, the effect of the air curtain is noted as the dispersion towards person 11 is hindered and hence, the higher concentration moves in lateral direction towards person 8. In cases 1 and 2 it takes around 5 min for the aerosol cloud to reach the furthest persons from the source. In case 3, it takes almost 7 min to reach even the closest person 6 (ii), and 12 min to reach the second closest singer 2. The concentration levels in case 3 at the singers neighboring the source

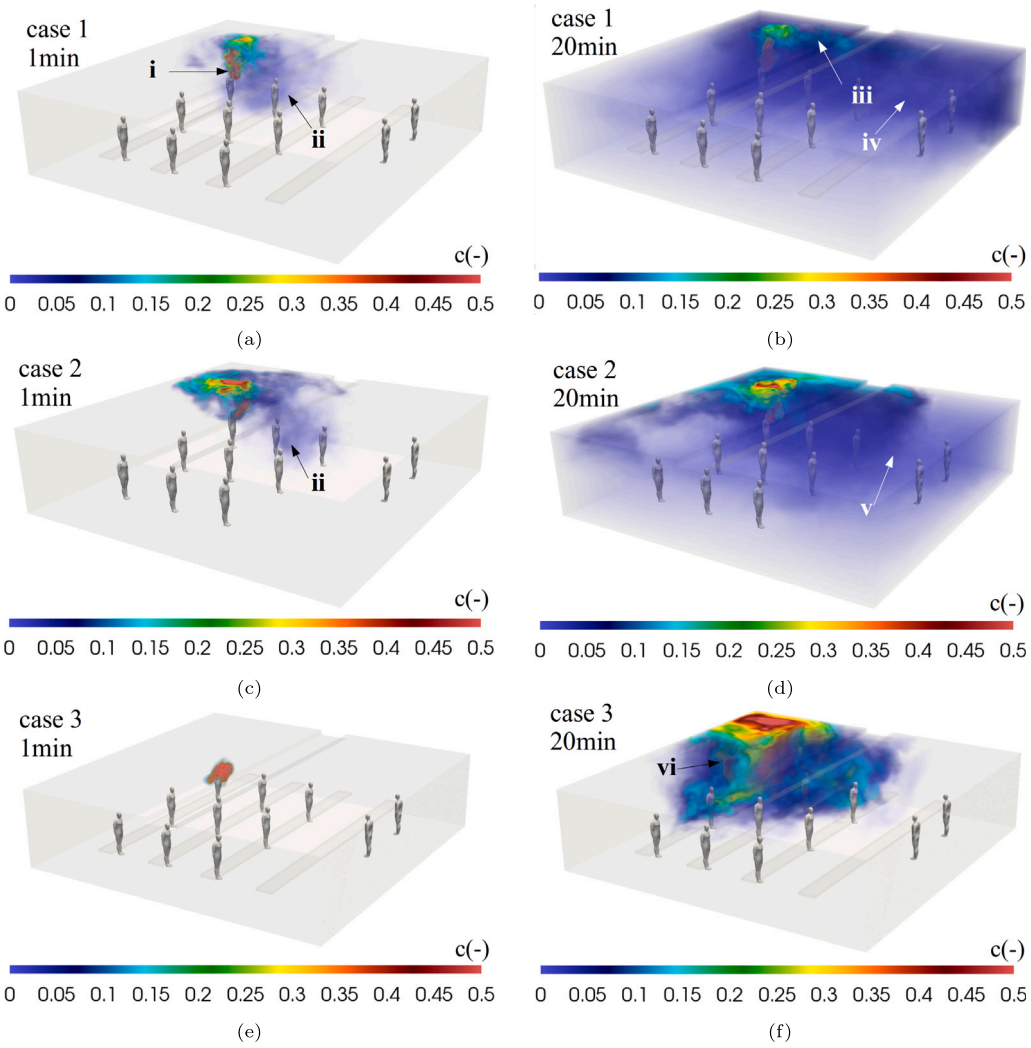

Fig. 8. Visualization of the aerosol dispersion from the initial source. (a) Case 1 at $t = 1$ min, (b) Case 1 at $t = 20$ min, (c) Case 2 at $t = 1$ min, (d) Case 2 at $t = 20$ min, (e) Case 3 at $t = 1$ min, (f) Case 3 at $t = 20$ min. i: upward flow due to buoyancy, ii: downward flow from the inflow, iii: higher concentration near the ceiling, iv: bending of the inflow pushing the aerosols to the opposite end of the room, v: air curtain induced by the inflow retarding the dispersion of the aerosols, vi: upward flow induced by a large vortex.

are higher compared to cases 1 and 2, since the concentrations accumulate near the source due to poor mixing. The poor level of mixing in case 3 may be related to the absence of the buoyancy-driven flow structures that generate turbulence. It may be also noted, that the volumetric average concentration in case 3 exceeds the equilibrium concentration based on the assumption of perfect mixing. It is noteworthy that in case 3 the concentration is non-negligible only in the vicinity of the singers nearest to the source (persons 2, 5, 6 and 9), while in cases 1 and 2 all singers appear to be exposed to a non-zero concentration level. However, the slow dispersion of the aerosols in case 3 is considered to be a result of incomplete modeling of air currents, in particular buoyant plumes, in the vicinity of the source. Consequently, incomplete turbulent dispersion is observed. In cases 1, 2 and 3 a total of 70%, 90% and 40% of the choir attendees were exposed to over 1% concentration levels within the 20 min simulation time, respectively. In the context of super-spreading events, the present numerical results indicate that the potential concentration threshold for infection may be rather low if the residence time is long enough.

The inhalation dose can be considered to be proportional to the product of the concentration level and the exposure time [1,41]. Fig. 12 shows the cumulative dose of the respiratory aerosols for each participant with respect to time. The dose is normalized by the concentration level of 1 at the source. The cumulative value is proportional to the inhalation dose of the respiratory aerosols, and not the virus dose. We acknowledge that the value presented here is of numerical character, and does not necessarily correlate directly with the infection risk. The figure indicates significantly higher dose of the respiratory aerosols for singer 6 in cases 1 and 2, while in case 3 the highest cumulative dose is for singers 6 and 2. Fig. 12 shows similar trend as noted in Fig. 11 for the concentrations of each participant. As a remark, in cases 1 and 2 the aerosol dose increases almost linearly with time after $t = 5$ min, further indicating the rapid mixing and turbulent dispersion of the aerosol concentration.

Comparing the dispersion of the respiratory aerosols between the cases reveal a significant difference between case 3 and the two other cases. In particular, a comparison of case 1 and case 3 reveals the strong impact of buoyancy for aerosol dispersion in the same geometric configuration. However, the differences between cases 1 and 2 remain less pronounced. The state of the indoor air is dependent on heating and the level of occupancy, in addition to the furniture. Considering the linkage of the present numerical findings to a known super-spreading event, which motivated the present study, our results indicate that long enough exposure to even small concentration levels of e.g. 1% relative to the aerosol concentration at the source may lead to a SARS-CoV-2 infection. In the present study, such an exposure level may be reached in less than 20 min time. Our results here are scalable and not only

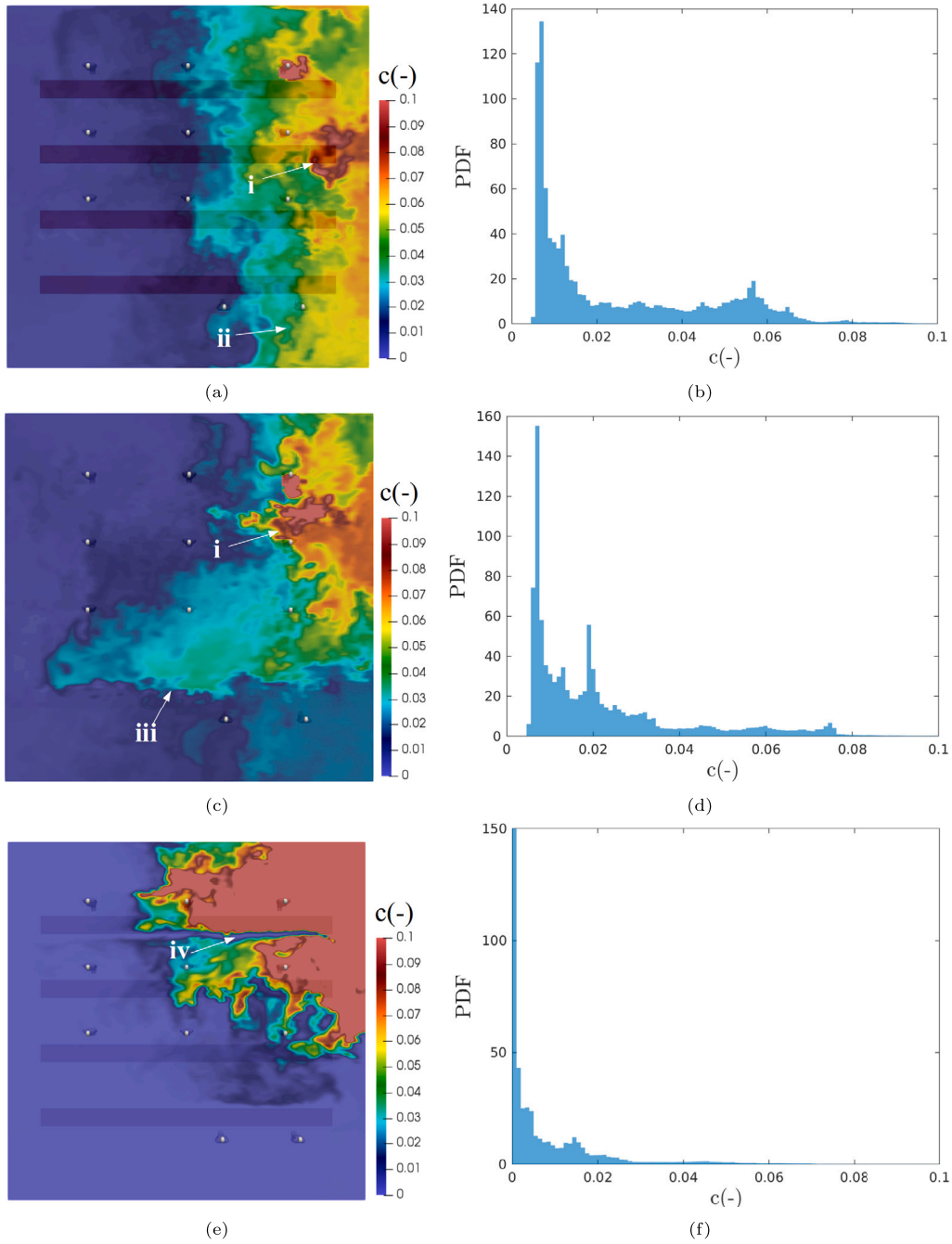

Fig. 9. Visualization of the aerosol concentration at the breath level for (a) Case 1, (c) Case 2 and (e) and Case 3, and PDF of the concentration at the breath level for (b) Case 1, (d) Case 2 and (f) Case 3. i: Higher concentration due to the downward flow of the inflow, ii: aerosols being pushed to the opposite side of the room due to the bending of the inflow jets, iii, iv: air curtain hindering the dispersion of the aerosols.

limited to singing. For example, the level of aerosol emission has been shown to be reduced by up to 90% by wearing masks [42]. In addition, the type of exhalation, i.e. speaking, singing, breathing, is known to affect the respiratory aerosol emission [43]. In the present study we assumed that the precise details of the exhalation activity (e.g. singing, speaking, or wearing a mask) may not have a significant effect on the overall indoor flow field which is more affected by the ventilation and thermal sources.

Regarding the modeling approach, LES was shown to capture the transitional flow features which obviously affect the turbulent dispersion of the aerosols. By using the more conventional RANS approach, the unsteady features of the transitional flows would need additional modeling. With LES, the transition and turbulent dispersion are resolved. In addition, Pope's criterion [39] was used to show that the LES was well resolved in Appendix B. Based on certain previous studies related to buoyancy-driven flows [23,25,26], it is known that LES can capture the inherently unsteady features exhibited herein, while RANS is considered to pose certain limitations. However, as a trade-off, the computational effort with LES compared to RANS is significantly higher in terms of computational effort. Here, for example, the present LES simulations took approximately 3 days with approximately 800 CPU's for each case when started from a fully developed flow field.

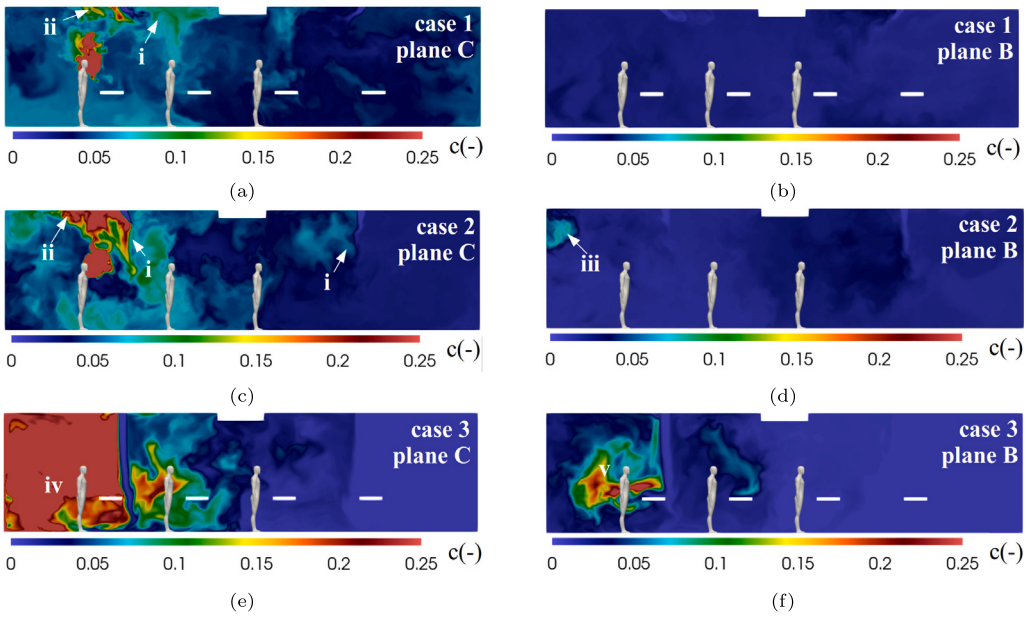

Fig. 10. The scalar concentration fields for cases 1-3 over plane C (infected singer) and plane B. i: transport of aerosols from the ceiling via the downward inflow. ii: accumulation of aerosols at the ceiling level. iii: aerosols trapped in a corner vortex. iv: aerosols accumulating in a large vortex in the proximity of the infected singer. v: aerosols trapped in a large vortex.

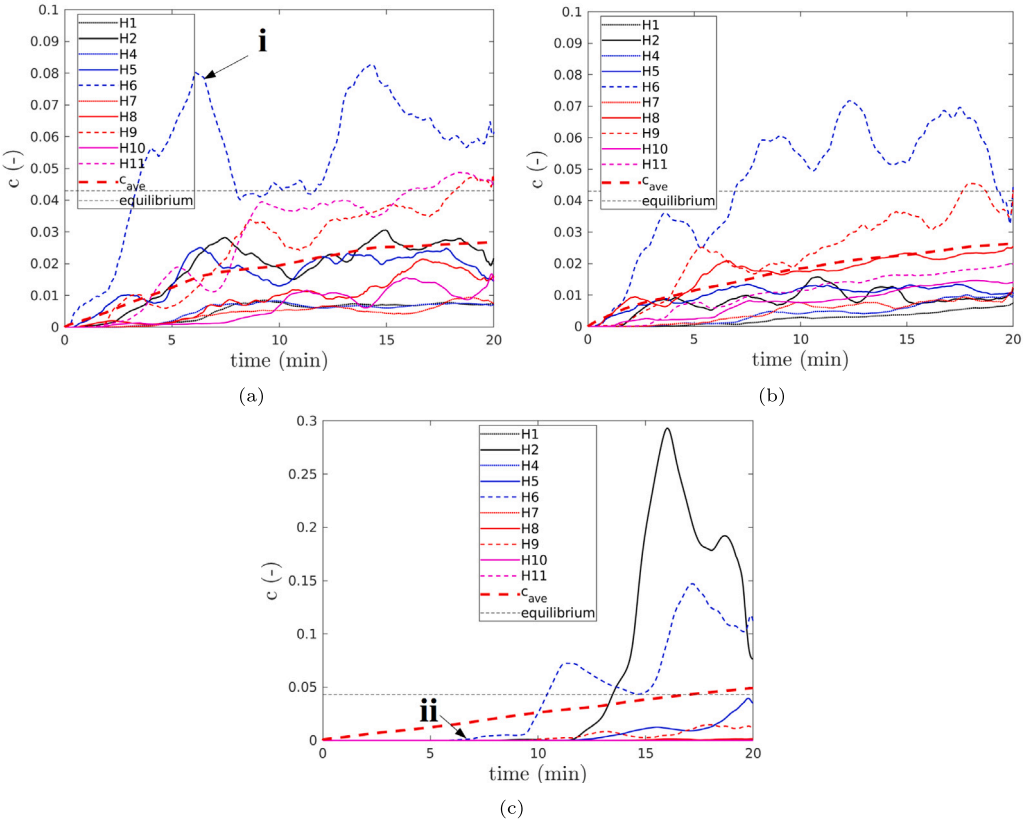

Fig. 11. Local average aerosol concentrations from the initial source at the locations of each human with respect to time, in addition to volumetric average over the entire room and an equilibrium concentration in perfect mixing conditions. (a) Case 1, (b) Case 2, (c) Case 3. i: A peak concentration due to the downward flow from the inflow, ii: minor increase in concentration.

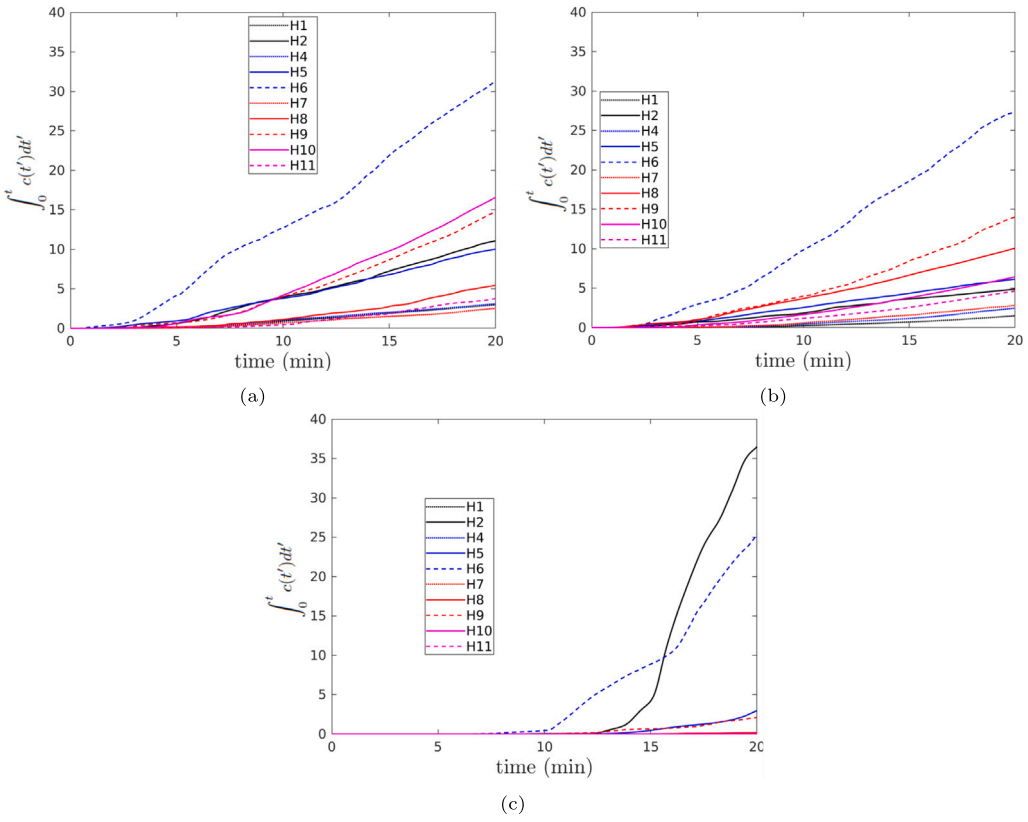

Fig. 12. Cumulative average aerosol doses from the initial source at the locations of each human with respect to time. (a) Case 1, (b) Case 2, (c) Case 3.

4. Conclusions

A large scale room CFD simulation was carried out using LES. The mixing ventilation setup had ACH=3.5 and the thermal sources from the radiators and choir attendees was taken into account. One of the limitations of the present volumetric heating model is that it does not take thermal/viscous surface boundary layers into account near the heat sources. However, one of the benefits of the present model is to precisely determine the heating power (W) and in this way also to account for buoyancy effects by the emerging thermal plumes. The case was simulated in three different conditions: case (1) full setup with all the heat sources and tables, case (2) without the heat source from the radiators and without tables, and case (3) case 1 under isothermal flow assumption. Altogether eleven singers were taken into account assuming a single infected source located in one of the corners of the room. The simulated case is motivated by a real life choir practice incidence where all attendees were thought to be infected by a single infected person implying aerosol transmission. The spreading of the fine aerosols from the infected singer was studied with a passive scalar concentration field.

The main findings of the paper are as follows. First, the turbulent flow patterns in the room were noted to be highly affected by the thermal plumes from the singers and the radiators (case 1). This was further demonstrated by simulating the room without the radiators and furniture (case 2), as well as a room without heat sources and uniform temperature (case 3). The absence of the radiators changed the cooler inflow originated flow structures significantly, indicating that the thermal plumes from the radiators are highly relevant to the overall flow patterns. However, the key difference was noted to be between cases 1 and 3 i.e. when the buoyancy was deactivated in the numerical simulations.

Second, as expected, the aerosol dispersion was noted to follow the observed flow structures. However, since the inflow based Reynolds number was relatively low in all cases, the dispersion in case 3 without buoyancy was highly different compared to cases 1-2 where buoyancy was taken into account. The buoyancy was noted to clearly increase the turbulence and hence, the mixing and dispersion. Such complicated physical phenomena require scale-resolving approaches such as LES or DNS for capturing the flow with laminar, transitional, and fully turbulent flow parts. In case 3, after 20 min, the aerosol cloud had reached only the closest singers from the source. In case 1-2, where buoyancy was taken into account, the aerosol cloud reached the furthest singers from the source in less than 5 min. As the present numerical study indicates, the importance of buoyancy is evident in accurate indoor airflow simulations. However, taking general uncertainty into account in future investigation may be of very high relevance as room occupancy, location of the furniture, and seasonal aspects are commonly changing.

The present results demonstrate the complexity of the flow features occurring in a ventilated room. Designing of the ventilation strategy is a multi-disciplinary task, where the heating and decoration, as well as the room occupancy have a significant effect on the air quality. For airborne pathogens, such as SARS-CoV-2 or influenza viruses, good air quality is also considered to be of key importance in reducing the infection risk by virus-laden aerosols. However, we note that the present results are of numerical character and specific to the studied flow setups. In future studies aspects such as flow Reynolds number and different thermal source configurations could be further investigated. The development of high resolution CFD methods together with uncertainty assessment methods over different ensembles of ventilation strategies, location of thermal sources and geometrical configurations may be an emerging research area.

CRediT authorship contribution statement

Alpo Laitinen: Writing – original draft, Visualization, Validation, Software, Methodology, Formal analysis. **Marko Korhonen:** Writing

– review & editing, Validation, Software. **Karri Keskinen:** Writing – review & editing, Validation, Software. **Ossi Kaario:** Writing – review & editing. **Ville Vuorinen:** Writing – review & editing, Supervision.

Declaration of competing interest

The authors declare that they have no known competing financial interests or personal relationships that could have appeared to influence the work reported in this paper.

Data availability

The authors do not have permission to share data.

Acknowledgments

This work was partially funded by Academy of Finland (grant No. 335516). The computational resources for this study were provided by CSC Finnish IT Center for Science.

Appendix A. Validation case: buoyant cavity

The buoyant cavity is a canonical case for investigating natural convection flows in a closed container with temperature-controlled sidewalls. The simulation case is ran with four different meshes to confirm grid independence, and the results are compared to experimental results reported by Betts and Bokhrai [38]. The dimensions of the cavity and the thermal boundary conditions are similar to the experimental set-up. The mesh resolutions used here are 80k, 160k, 370k and 630k cells. The instantaneous and time-averaged velocity and temperature fields of the buoyant cavity for the finest mesh are displayed in Fig. A.13. The air at the heated wall becomes warmer, experiences a net buoyancy and travels up towards the cavity ceiling. Contrarily, the cooled air at the opposite wall descends towards the bottom. Additionally, sporadic vortices indicative of turbulent phenomena are present along the walls provided that the Rayleigh number is sufficiently high.

Fig. A.14 illustrates the temporally averaged streamwise velocity component and temperature across the cavity width along line plots at $y = 0.9$H and $y = 0.1$H. The time-averaged velocity and temperature profiles exhibit a good agreement between the simulations and the experiments with all meshes, indicating that sufficient results are obtained even with the coarsest mesh. The good agreement between the experimental and numerical results confirm that the present numerical model produces physically valid results.

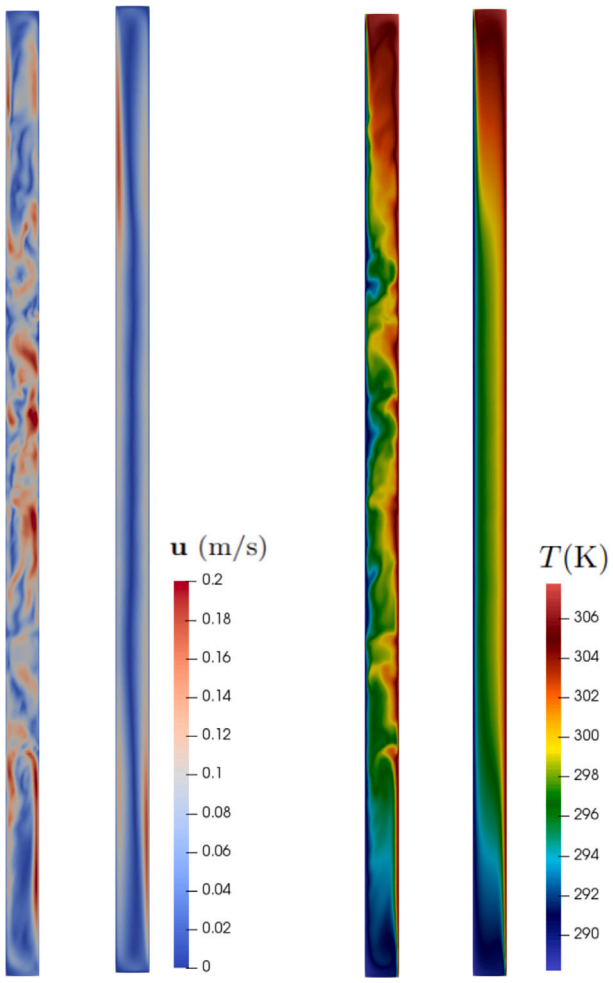

Fig. A.13. Figure of the instantaneous and time-averaged velocity (left) and temperature (right) fields.

Appendix B. Grid convergence study

The previous validation case provides evidence that the present LES method produces physically valid results. However, in addition to prove the capability to replicate a reference case with an arbitrarily fine mesh, a mesh sensitivity study of the present case configuration is provided to verify the numerical methods. The grid sensitivity analysis is shown with OpenFOAM. The present grid consists of hexagonal cells of various sizes. An illustrative figure of the grid can be seen in Fig. B.15. Fig. B.15(a) shows a cut-plane over which the results for the grid convergence study are shown. Fig. B.15(b) shows the structure of the grid. The grid is refined around the tables, at the locations of the heat sources, and near the walls. Each refinement region halves the cell size, i.e. for a base cell size of Δx_b, first refinement region is $\Delta x_b/2$ and the second is $\Delta x_b/4$. For the coarsest mesh, the base cell size is $\Delta x_b = 0.04$ m, resulting in $\Delta x = 0.01$ m being the smallest cell size, while the finest mesh is half from this, i.e. the finest cell in the finest mesh is $\Delta x = 0.005$ m. The first refinement is at the locations of the heat sources, and further away from the walls. The second refinement is near the walls, as seen in the figure. In the longitudinal direction of the tables, no refinement is added to reduce the computational effort. This is justified, since the velocities in this direction are negligibly small compared to the other directions. The different meshes are created by varying the base cell size, and the corresponding cell numbers are 3.4M, 7.7M, 13.2M and 25.5M. The grids are generated with the commercial software STAR-CCM+.

The time-averaged velocity field over the cut-plane (see Fig. B.15(a)) for each of the grid resolutions can be seen in Fig. B.16. The velocity field shows the inflow air (i), buoyancy generated by the radiator (ii), and the buoyancy generated by the singers (iii) with all grid resolutions. In the large scale structures, not much difference can be seen between the different resolutions. This indicates, that the time-averaged large scale flow features are less dependent on the mesh quality.

Fig. B.17 shows the instantaneous temperature field for each mesh. Here it is noted, that the instability from the rising warm air (i) is not properly generated with the coarser grid resolutions. This indicates that the small scale fluctuations may not be properly captured with the 3.4M and 7.7M meshes. It can be observed in the figure, that the buoyancy generated by the temperature differences are mostly driving the flow. This indicates that an accurate prediction of the temperature field is necessary to obtain reliable results for the flow fields.

The ratio of the modeled turbulent kinetic energy k_{SGS} to the total turbulent kinetic energy $k_{tot} = k_{SGS} + k_{res}$, where $k_{res} = 1/2\sqrt{\overline{(u'_x)^2} + \overline{(u'_y)^2} + \overline{(u'_z)^2}}$, provides and indication on the grid resolution. The finer the grid, the smaller the ratio of the modeled part to the resolved part. A good ratio has been considered to be less than

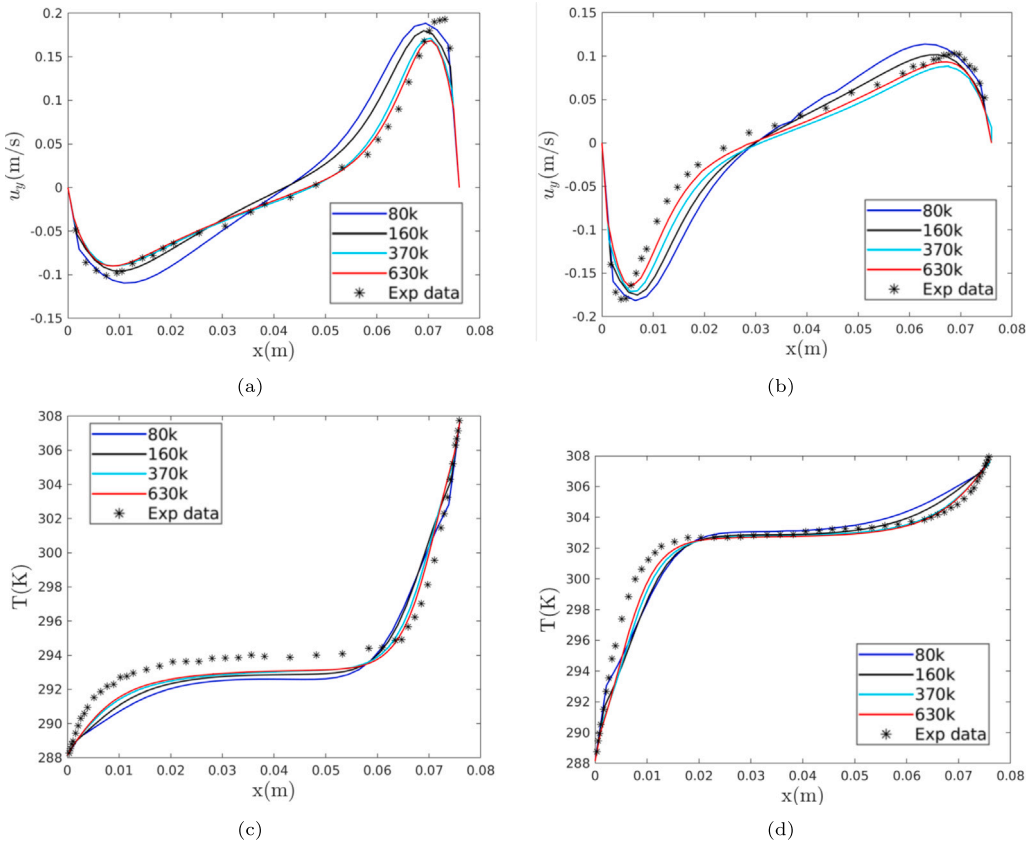

Fig. A.14. Plots of the time-averaged stream-wise velocity component at (a) $y = 0.1$H and (b) $y = 0.9$H, and the time-averaged temperature at (c) $y = 0.1$H and (d) $y = 0.9$H. The figure shows good agreement between the experiments and the simulations.

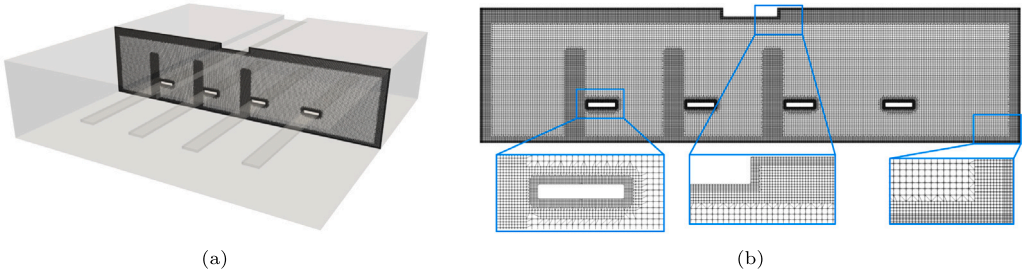

Fig. B.15. Figure of the mesh indicating the locations of the refinement regions.

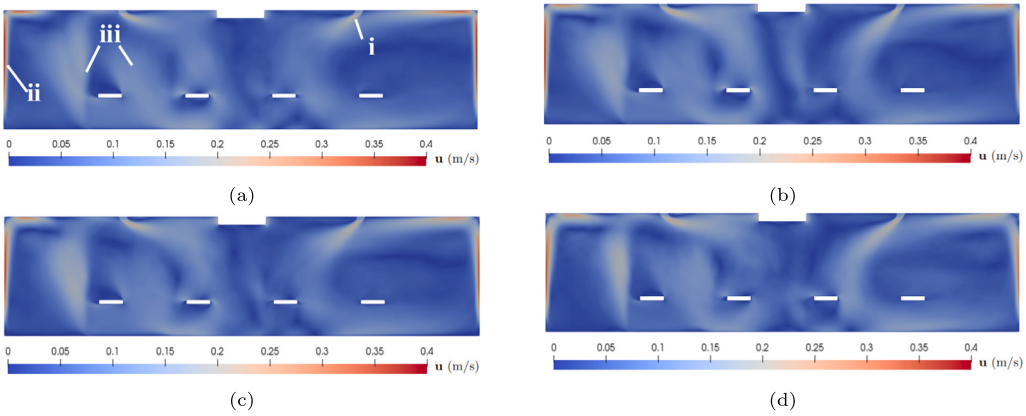

Fig. B.16. Comparison of the time-averaged velocity magnitude on a cut-plane for the different grid resolutions. (a): 3.4M cells, (b): 7.7M cells, (c): 13.2M cells, (d): 25.5M cells. i: inflow air, ii: buoyancy from the radiator, iii: buoyancy from the singers.

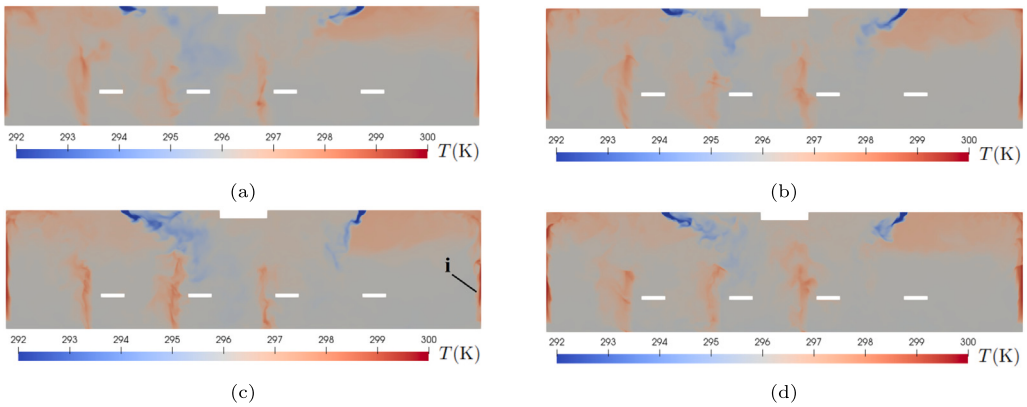

Fig. B.17. Comparison of the instantaneous temperature on a cut-plane for the different grid resolutions. (a): 3.4M cells, (b): 7.7M cells, (c): 13.2M cells, (d): 25.5M cells. i: instability.

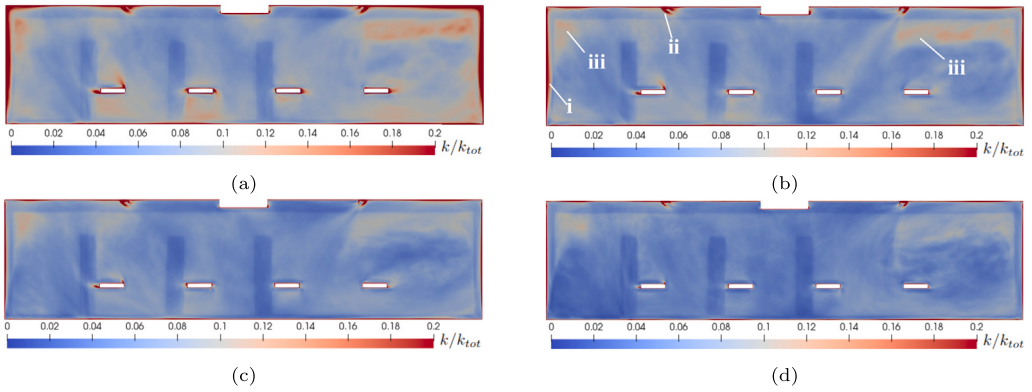

Fig. B.18. Comparison of the Pope criterion on a cut-plane for the different grid resolutions. (a): 3.4M cells, (b): 7.7M cells, (c): 13.2M cells, (d): 25.5M cells. i: instability. (i): wall flow, (ii): shear layer of the inflow, (iii): regions where the buoyancy of the radiators mix with the inflow.

20% [39], which is referred to as the Pope criterion. Fig. B.18 shows the Pope criterion for each of the meshes. Generally, in most areas the ratio shows values below 20% with all the grids. The main difference is near the walls (i) and at the shear layer of the inflow air (ii), where the value exceeds the Pope criterion. In the regions where the buoyancy of the radiators mix with the inflow air (iii), the ratio is noted to be the second highest. It is noted, that no significant differences are observed between the 13.2M and 25.5M meshes.

The ratio of the eddy viscosity ν_T to the kinematic viscosity ν is shown in Fig. B.19. This ratio further indicates the portion of the SGS to the resolved results. It gives evidence to the level of the modeled turbulence. As can be seen in the figure, the ratio is the highest in the 3.4M cell case. Here, a greater difference is observed between the 13.2M and 25.5M meshes compared to the other indicators. However, the ratio in the 13.2M case is much less than 10, which indicates that the resolution is reasonably high and that the quality of the LES is good.

The present grid sensitivity study provides verification for the numerical results. With most indicators, no significant differences were observed between the 13.2M and 25.5M meshes. Even the 7.7M mesh gives reasonable accuracy based on most of the indicators. However, there is some instability noted in the instantaneous temperature field with the 13.2M mesh shows that the coarser meshes are not applicable for high quality simulations. Both 13.2M and 25.5M meshes passed each indicator, however, the 25.5M would significantly increase the already substantial computational cost. Hence, the 13.2M mesh is selected for the main simulations of the study. The grid convergence study in addition to the provided validation case creates confidence for the accuracy of the present study.

Appendix C. OpenFOAM vs. DNSLABIB

In addition to OpenFOAM, the thermally uniform case (case 3) is simulated with another solver, called DNSLABIB. DNSLABIB is a CFD solver implemented in MATLAB and capable of being executed on both GPU and CPU. Originally released in 2016 [40], the software implements the incompressible Navier–Stokes equations utilizing the Chorin-Temam projection method for solving the pressure field. The momentum equation is discretized with finite differencing (central differences) while the time integration is performed with the explicit 4th order Runge–Kutta method. Furthermore, the pressure equation is solved applying spectral methods and a 6th order hyperviscosity model is used as a filter for the velocity, rendering this approach essentially an implicit large-eddy simulation (ILES). The software has recently been augmented with the Immersed Boundary (IB) method to handle solid obstacles and walls [44].

The instantaneous and time-averaged velocity fields in addition to the turbulent kinetic energy for OpenFOAM and DNSLABIB simulations are presented in Fig. C.20. The large scale flow in the time-averaged fields is observed to be qualitatively similar with no major differences. In the instantaneous flow fields, it may be noted that the fluctuation of the jets is somewhat higher with DNSLABIB, and the small turbulent structures away from the jets are seemingly larger. The total turbulent kinetic energy for the OpenFOAM case is the sum of the resolved and SGS fields, while with the DNSLABIB there is no modeled part and it is all resolved. The level of turbulence in OpenFOAM is noted to be higher in the jet-wall impingement regions and in the mixing region of the inflow jets in the center of the room. This can be noted from the total

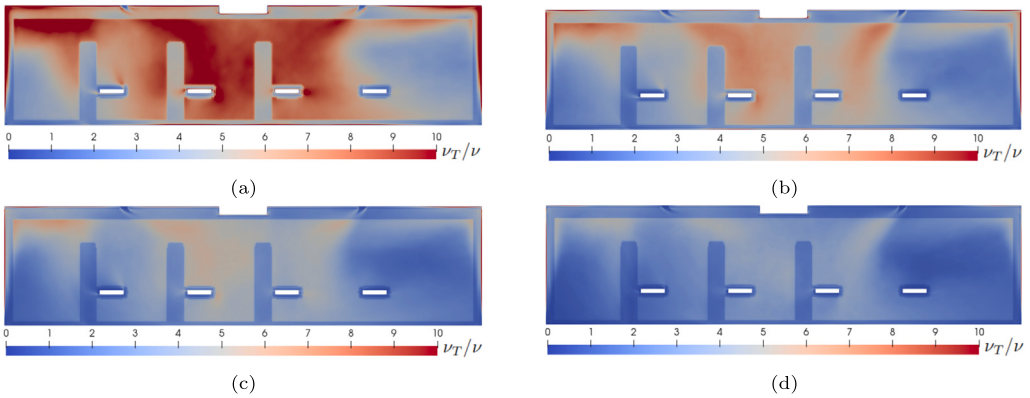

Fig. B.19. Comparison of the ratio of the eddy viscosity to the kinematic viscosity on a cut-plane for the different grid resolutions. (a): 3.4M cells, (b): 7.7M cells, (c): 13.2M cells, (d): 25.5M cells. i: instability.

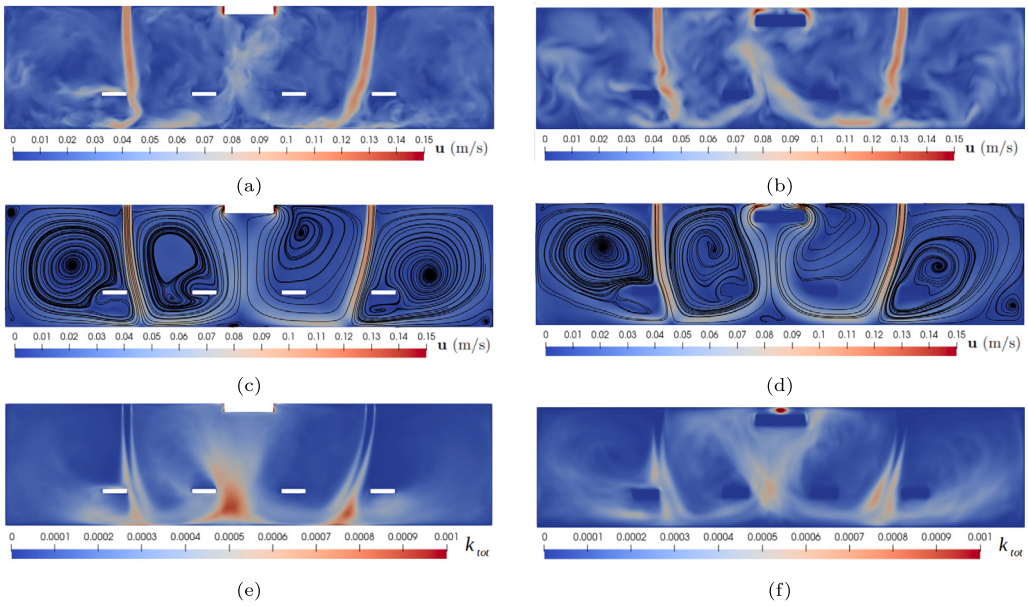

Fig. C.20. Instantaneous velocity fields with (a) OpenFOAM and (b) DNSLABIN, time-averaged velocity fields with (c) OpenFOAM and (d) DNSLABIB, and the turbulent kinetic energy with (e) OpenFOAM and (f) DNSLABIB over a central cut-plane for OpenFOAM and DNSLABIB simulations. The figure shows good agreement between the two different solvers.

turbulent kinetic energy as well as the structures in the instantaneous velocity field. Overall, the results between OpenFOAM and DNSLABIB are in good agreement with some differences in the small scale flows.

References

[1] V. Vuorinen, M. Aarnio, M. Alava, V. Alopaeus, N. Atanasova, M. Auvinen, N. Balasubramanian, H. Bordbar, P. Erästö, R. Grande, et al., Modelling aerosol transport and virus exposure with numerical simulations in relation to SARS-CoV-2 transmission by inhalation indoors, Saf. Sci. 130 (2020) 104866.

[2] C.C. Wang, K.A. Prather, J. Sznitman, J.L. Jimenez, S.S. Lakdawala, Z. Tufekci, L.C. Marr, Airborne transmission of respiratory viruses, Science 373 (6558) (2021) eabd9149.

[3] R. Tellier, COVID-19: the case for aerosol transmission, Interface Focus 12 (2) (2022) 20210072.

[4] World Health Organization, et al., COVID-19 transmission and protective measures, 2020, World Health Organization. At https://Www.Who.Int/Westernpacific/Emergencies/COVID-19/Information/Transmission-Protective-Measures.

[5] ASHRAE, ASHRAE position document on infectious aerosols, Peachtree Corners (2022).

[6] Z. Nie, Y. Chen, M. Deng, Quantitative evaluation of precautions against the COVID-19 indoor transmission through human coughing, Sci. Rep. 12 (1) (2022) 22573.

[7] L. Dye, Superspreading drives the COVID pandemic — and could help to tame it, Nature 590 (2021) 544–546.

[8] L. Borro, L. Mazzei, M. Raponi, P. Piscitelli, A. Miani, A. Secinaro, The role of air conditioning in the diffusion of sars-CoV-2 in indoor environments: A first computational fluid dynamic model, based on investigations performed at the vatican state children's hospital, Environ. Res. (2020) 110343.

[9] B. Blocken, T. van Druenen, A. Ricci, L. Kang, T. van Hooff, P. Qin, L. Xia, C.A. Ruiz, J. Arts, J. Diepens, et al., Ventilation and air cleaning to limit aerosol concentrations in a gym during the COVID-19 pandemic, Build. Environ. (2021) 107659.

[10] J. Ren, Y. Wang, Q. Liu, Y. Liu, Numerical study of three ventilation strategies in a prefabricated COVID-19 inpatient ward, Build. Environ. 188 (2021) 107467.

[11] F. Ascione, R.F. De Masi, M. Mastellone, G.P. Vanoli, The design of safe classrooms of educational buildings for facing contagions and transmission of diseases: A novel approach combining audits, calibrated energy models, building performance (BPS) and computational fluid dynamic (CFD) simulations, Energy Build. 230 (2021) 110533.

[12] X. Deng, G. Gong, X. He, X. Shi, L. Mo, Control of exhaled SARS-CoV-2-laden aerosols in the interpersonal breathing microenvironment in a ventilated room with limited space air stability, J. Environ. Sci. (2021).

[13] S. Bhattacharyya, K. Dey, A.R. Paul, R. Biswas, A novel CFD analysis to minimize the spread of COVID-19 virus in hospital isolation room, Chaos Solitons Fractals 139 (2020) 110294.

[14] Y. Li, P.V. Nielsen, CFD and ventilation research, Indoor Air 21 (6) (2011) 442–453.

[15] B. Blocken, LES over RANS in building simulation for outdoor and indoor applications: A foregone conclusion? in: Building Simulation, Vol. 11, No. 5, Springer, 2018, pp. 821–870.
[16] J. Jiang, X. Wang, Large eddy simulation of airflows in a full scale room at different ventilation rates., ASHRAE Trans. 115 (2) (2009).
[17] S. Liu, A. Novoselac, Lagrangian particle modeling in the indoor environment: A comparison of RANS and LES turbulence methods (RP-1512), HVAC&R Res. 20 (4) (2014) 480–495.
[18] D. Karadimou, N. Markatos, Modelling of two-phase, transient airflow and particles distribution in the indoor environment by large eddy simulation, J. Turbul. 17 (2) (2016) 216–236.
[19] H. Liu, S. He, L. Shen, J. Hong, Simulation-based study of COVID-19 outbreak associated with air-conditioning in a restaurant, Phys. Fluids 33 (2) (2021) 023301.
[20] G. Tu, W. Li, K. Du, G. Huang, F. Wang, Onset and influencing factors of deflecting oscillation in planar opposed jets, Chem. Eng. J. 247 (2014) 125–133.
[21] J.-H. Thysen, T. van Hooff, B. Blocken, G. van Heijst, CFD simulations of two opposing plane wall jets in a generic empty airplane cabin: Comparison of RANS and LES, Build. Environ. 205 (2021) 108174.
[22] D. Etheridge, A perspective on fifty years of natural ventilation research, Build. Environ. 91 (2015) 51–60.
[23] Y. Huang, G. Yang, J. Wu, Large eddy simulation and experimental study of turbulent mixed convection inside a cavity with large Rayleigh number: Effect of buoyancy, Build. Environ. 151 (2019) 268–279.
[24] L.W. Chew, C. Chen, C. Gorlé, Improving thermal model predictions for naturally ventilated buildings using large-eddy simulations, Build. Environ. (2022) 109241.
[25] F. Durrani, M.J. Cook, J.J. McGuirk, Evaluation of LES and RANS CFD modelling of multiple steady states in natural ventilation, Build. Environ. 92 (2015) 167–181.
[26] M. Caciolo, P. Stabat, D. Marchio, Numerical simulation of single-sided ventilation using RANS and LES and comparison with full-scale experiments, Build. Environ. 50 (2012) 202–213.
[27] M. Auvinen, J. Kuula, T. Grönholm, M. Sühring, A. Hellsten, High-resolution large-eddy simulation of indoor turbulence and its effect on airborne transmission of respiratory pathogens—Model validation and infection probability analysis, Phys. Fluids 34 (1) (2022) 015124.
[28] A. Laitinen, K. Saari, K. Kukko, P. Peltonen, E. Laurila, J. Partanen, V. Vuorinen, A computational fluid dynamics study by conjugate heat transfer in openfoam: A liquid cooling concept for high power electronics, Int. J. Heat Fluid Flow 85 (2020) 108654.
[29] A. Laitinen, E. Laurila, K. Keskinen, V. Vuorinen, Large-eddy simulation of two secondary air supply strategies in kraft recovery boilers, Appl. Therm. Eng. 216 (2022) 119035.
[30] H.G. Weller, G. Tabor, H. Jasak, C. Fureby, A tensorial approach to computational continuum mechanics using object-oriented techniques, Comput. Phys. 12 (6) (1998) 620–631.
[31] R.I. Issa, Solution of the implicitly discretised fluid flow equations by operator-splitting, J. Comput. Phys. 62 (1) (1986) 40–65.
[32] S.V. Patankar, D.B. Spalding, A calculation procedure for heat, mass and momentum transfer in three-dimensional parabolic flows, in: Numerical Prediction of Flow, Heat Transfer, Turbulence and Combustion, Elsevier, 1983, pp. 54–73.
[33] A. Hartan, High resolution schemes for hyperbolic conservative laws, J. Comput. Phys. 49 (1983) 357–393.
[34] A. Yoshizawa, Statistical theory for compressible turbulent shear flows, with the application to subgrid modeling, Phys. Fluids 29 (7) (1986) 2152–2164.
[35] B.E. Launder, D.B. Spalding, The numerical computation of turbulent flows, in: Numerical Prediction of Flow, Heat Transfer, Turbulence and Combustion, Elsevier, 1983, pp. 96–116.
[36] W. Feist, What is a Passive House, Passive House Institute, 2007, pp. 2–3.
[37] American National Standards Institute, Thermal Environmental Conditions for Human Occupancy, Vol. 55, No. 2004, American Society of Heating, Refrigerating and Air-Conditioning Engineers, 2004.
[38] P. Betts, I. Bokhari, Experiments on turbulent natural convection in an enclosed tall cavity, Int. J. Heat Fluid Flow 21 (6) (2000) 675–683.
[39] S.B. Pope, Ten questions concerning the large-eddy simulation of turbulent flows, New J. Phys. 6 (1) (2004) 35.
[40] V. Vuorinen, K. Keskinen, DNSlab: A gateway to turbulent flow simulation in matlab, Comput. Phys. Comm. 203 (2016) 278–289.
[41] Z. Wang, E.R. Galea, A. Grandison, J. Ewer, F. Jia, A coupled computational fluid dynamics and wells-riley model to predict COVID-19 infection probability for passengers on long-distance trains, Saf. Sci. 147 (2022) 105572.
[42] S. Asadi, C.D. Cappa, S. Barreda, A.S. Wexler, N.M. Bouvier, W.D. Ristenpart, Efficacy of masks and face coverings in controlling outward aerosol particle emission from expiratory activities, Sci. Rep. 10 (1) (2020) 1–13.
[43] S. Asadi, A.S. Wexler, C.D. Cappa, S. Barreda, N.M. Bouvier, W.D. Ristenpart, Aerosol emission and superemission during human speech increase with voice loudness, Sci. Rep. 9 (1) (2019) 1–10.
[44] M. Korhonen, A. Laitinen, G.E. Isitman, J.L. Jimenez, V. Vuorinen, A GPU-accelerated computational fluid dynamics solver for assessing shear-driven indoor airflow and virus transmission by scale-resolved simulations, 2022, http://dx.doi.org/10.48550/ARXIV.2204.02107, URL https://arxiv.org/abs/2204.02107.